Electronic structure of the kagome metal $YbTi_3Bi_4$ studied using torque magnetometry

Kyryl Shtefiienko,[1,*] Cole Phillips,[1,*] Brenden R. Ortiz,[2] David E. Graf,[3,4] and Keshav Shrestha[1,†]
[1]*Department of Chemistry and Physics, West Texas A&M University, Canyon, Texas 79016, USA*
[2]*Materials Science and Technology Division, Oak Ridge National Laboratory, Oak Ridge, Tennessee 37831, USA*
[3]*Department of Physics, Florida State University, Tallahassee, Florida 32306, USA*
[4]*National High Magnetic Field Laboratory, Tallahassee, Florida 32310, USA*

(Received 15 October 2024; revised 21 December 2024; accepted 8 January 2025; published 23 January 2025)

This study investigates the electronic structure of the kagome metal $YbTi_3Bi_4$ using high-field torque magnetometry. The torque signal measured at a maximum field of 41.5 T reveals clear de Haas–van Alphen (dHvA) oscillations with a major frequency peak at $F_\delta \sim 130$ T. By rotating the sample at various tilt angles θ, we observed that F_δ exhibits a nearly $1/\cos\theta$ dependence, indicating the presence of a quasi-two-dimensional (2D) Fermi surface (FS) in $YbTi_3Bi_4$. This argument is further supported by the detection of a forward-leaning, sawtoothlike waveform in the dHvA effect, a hallmark of 2D FS characteristics. Notably, we identified two high-frequency peaks near $F_\chi \sim 1900$ T and $F_\lambda \sim 5600$ T; however, these peaks quickly disappear at θ greater than 21°. To better understand experimental observations, we computed the electronic band structure and FS using *ab initio* density-functional theory (DFT). The electronic bands reveal the presence of several Dirac points, flat bands, and van Hove singularities near the Fermi level. Five bands cross the Fermi level and contribute to the FS of this material. The FS comprises cylindrical sheets, with theoretical frequencies from the FS pockets aligning well with the experimental dHvA frequencies. Several FS parameters characterizing F_δ were determined by analyzing the temperature and field dependence of the dHvA oscillations using the Lifshitz-Kosevich theory. The detailed electronic properties presented in this work provide critical insights into the electronic structure of $YbTi_3Bi_4$ and other titanium-based kagome compounds.

DOI: 10.1103/PhysRevB.111.035145

I. INTRODUCTION

Kagome materials have attracted significant research interest due to their intriguing physical and electronic structures, which include features such as charge-density wave (CDW) phenomena, nontrivial topology, Dirac points, saddle points, flat bands, and more [1–3]. These materials feature a quasi-two-dimensional (2D) lattice structure resembling a traditional Japanese basket-weaving pattern [4]. One notable example is the vanadium-based family AV_3Sb_5 (A = K, Rb, and Cs), also known as the 135 family, which forms a hexagonal lattice of V atoms coordinated by Sb atoms [5–7]. This family exhibits a range of exotic quantum phenomena, including superconductivity with critical temperatures (T_c) ranging from 0.3 to 3 K, CDW order near $T_{CDW} \sim 80$–110 K, nontrivial topology, a van Hove singularity and more [8–12]. The coexistence of nontrivial topology and superconductivity in AV_3Sb_5 makes these materials potential candidates for exploring topological superconductivity and Majorana fermions. Our group, along with others, has performed quantum oscillation studies to map the Fermi surface (FS) of AV_3Sb_5 [13–23].

Additionally, another vanadium-based family, RV_6Sn_6 (R = Rare earth), known as the 166 compounds, has been discovered [24–31]. Among these, GdV_6Sn_6, HoV_6Sn_6, and YV_6Sn_6 have been found to exhibit topological properties [26,32]. ScV_6Sn_6 is the only member of the 166 family to display CDW order below $T_{CDW} = 92$ K [31,33], although no superconductivity has been observed in ScV_6Sn_6 under ambient conditions or pressures up to 11 GPa [34]. It is important to note that a density wavelike transition has been recently reported in $LuNb_6Sn_6$ [35]. A different class of Ti-based kagome systems, ATi_3Bi_5 (where A = Cs, Rb) [36–38], crystallizes in the same structure as AV_3Sb_5, but with Ti atoms forming the kagome net instead of V, and Bi substituting for Sb. Unlike AV_3Sb_5, the ATi_3Bi_5 system shows no evidence of the CDW order or superconductivity (SC). Another recently synthesized Ti-based kagome system, $LnTi_3Bi_4$ (Ln = Lanthanides) [39,40], adopts an orthorhombic structure with the $Fmmm$ space group (No. 69). The unit cell has four kagome layers of the Ti sublattice, as shown in Figs. 1(a) and 1(b). Unlike the previously studied AV_3Sb_5 and ATi_3Bi_5 compounds, $LnTi_3Bi_4$ features slightly distorted kagome lattices and zigzag Ln chains within *Ln-Bi* bilayers. The density-functional theory (DFT) and angle-resolved photoemission spectroscopy (ARPES) studies [41–45] find the presence of van Hove singularities and Dirac points near the Fermi level of this material. Due to the presence of magnetism in rare earth elements in $LnTi_3Bi_4$, it is a suitable system for tuning magnetism by rare-earth engineering. Electrical transport and magnetic properties of this family have recently been reported, both at ambient conditions and under pressure [46–48]. Among this family, $YbTi_3Bi_4$

*These authors contributed equally to this work.
†Contact author: kshrestha@wtamu.edu

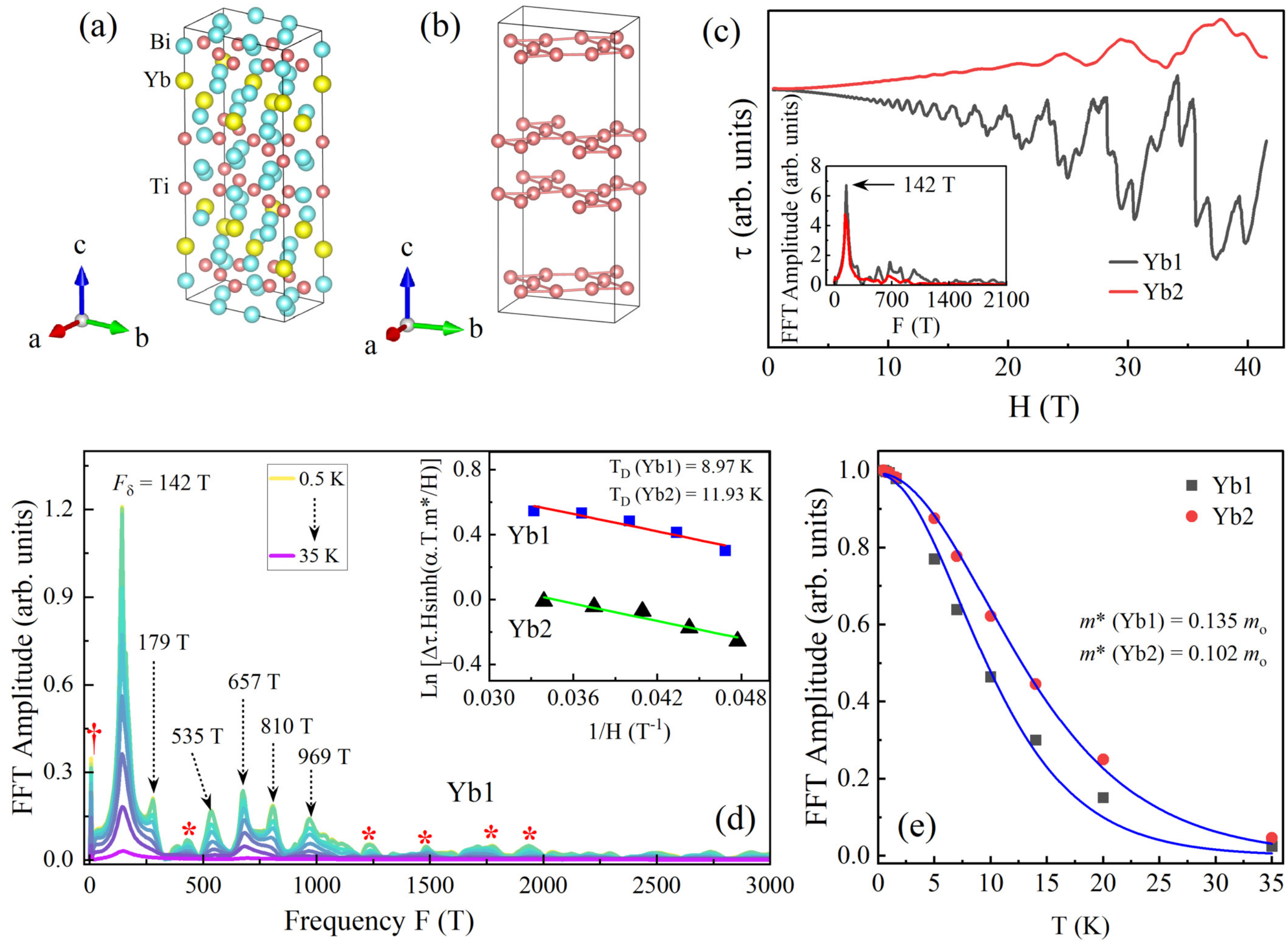

FIG. 1. (a) Unit cell of $YbTi_3Bi_4$. (b) Kagome layers of the Ti lattice within the unit cell. (c) Torque τ signal for two $YbTi_3Bi_4$ single crystals (Yb1 and Yb2) up to 41.5 T at $\theta = 28^\circ$ and $T = 0.5$ K, showing clear dHvA oscillations above 4 T. Inset: Frequency spectra of the dHvA oscillations for Yb1 and Yb2, displaying similar spectra with a major frequency peak at $F_\delta = 142$ T. (d) Temperature dependence of the frequency spectrum for Yb1, revealing six well-defined frequency peaks. Inset: Dingle temperature analysis for Yb1 and Yb2 of F_δ, where scattered data are experimental data and the solid lines are the best fits. (e) Lifshitz-Kosevich analysis of the temperature-dependent frequency data for Yb1 and Yb2.

and $LaTi_3Bi_4$, along with $CaTi_3Bi_4$, are the only members known to exhibit nonmagnetic properties. This is due to the valence states of Yb^{2+}, Ca^{2+}, and La^{3+}. No superconducting, structural, or electronic instabilities are observed down to 60 mK in $Ln$$Ti_3Bi_4$ [39,42].

A detailed understanding of the FS is essential for grasping the electronic properties of $Ln$$Ti_3Bi_4$. Despite several ARPES and DFT studies, quantum oscillation studies to map the FS properties of $Ln$$Ti_3Bi_4$ have not been reported. In this study, we conducted torque magnetometry measurements with applied fields up to 41.5 T to map the electronic structure of $YbTi_3Bi_4$. We observed a major peak at $F_\delta \sim 130$ T in the de Haas–van Alphen (dHvA) oscillations. By rotating the sample in the magnetic field, we successfully mapped the FS of F_δ. Interestingly, the dHvA oscillations exhibit a forward-leaning sawtoothlike wave form, clearly indicating the presence of a 2D FS in $YbTi_3Bi_4$. To support the experimental observations, we computed the electronic bands and FS using DFT. Our DFT calculations reveal several Dirac points, flat bands, and van Hove singularities near the Fermi level, along with quasi-2D FS sheets, consistent with the experimentally observed nearly $1/\cos\theta$ dependence of F_δ.

II. EXPERIMENTAL AND COMPUTATIONAL DETAILS

$YbTi_3Bi_4$ single crystals are grown through a bismuth self-flux. Yb metal (Ames) (Alfa 99.5%), Ti powder (Alfa 99.9%), and Bi shot (Alfa 99.999% low-oxide) were placed into a $\sim$5 mL Canfield crucible fitted with a catch crucible and a porous frit [49] at a ratio of 2:3:20 = Yb:Ti:Bi. The crucibles were sealed under approximately $\sim$0.7 atm of argon gas in fused silica ampoules. Samples were heated to 1100 °C at a rate of 200 °C/hr and thermalized at 1100 °C for 12 h. The growth proceeded with a cooling rate of 2 °C/hr to 600 °C. Excess bismuth was removed through centrifugation at 600 °C. Resulting crystals are pseudohexagonal plates with typical dimensions ranging from $1 \times 1 \times 0.2$ mm^3 to $5 \times 5 \times 1$ mm^3. Crystals have a

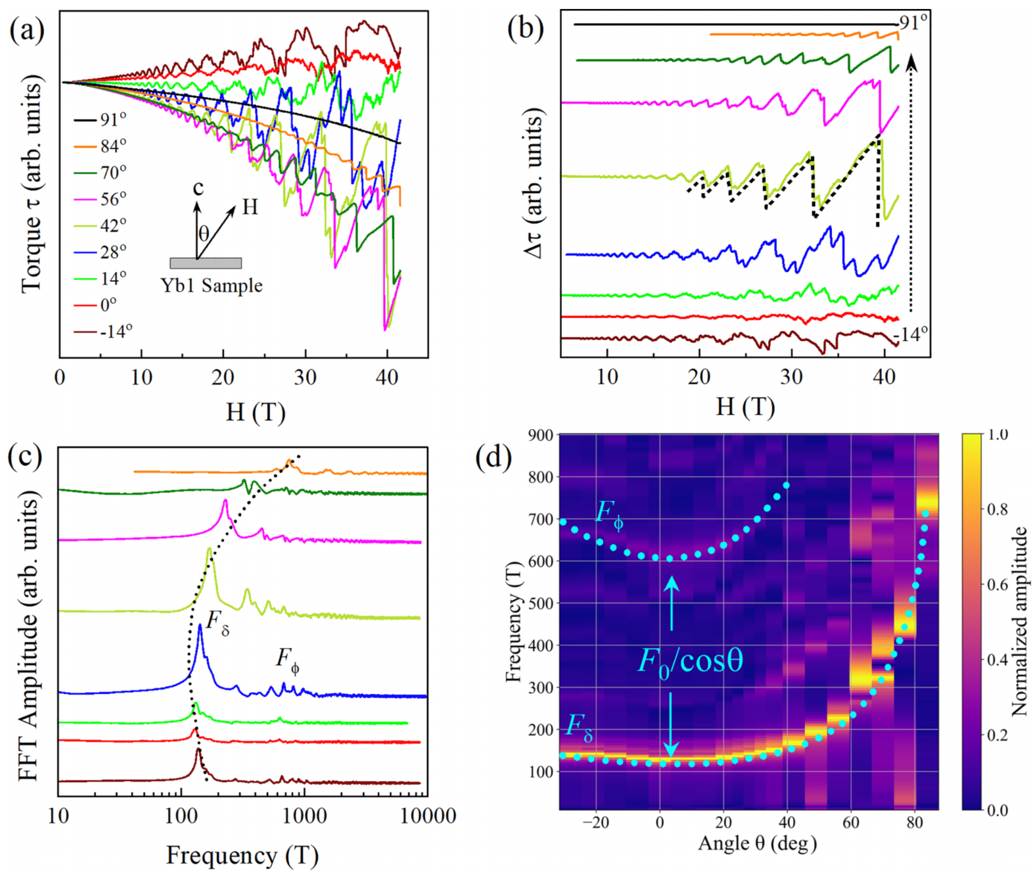

FIG. 2. (a) Angular dependence of dHvA oscillations for the $YbTi_3Bi_4$ (Yb1 sample) measured at $T = 0.5$ K. The tilt angle θ is defined as the angle between the magnetic field and the c axis. (b) Background-subtracted torque data showing how the amplitude and period of quantum oscillations change with θ. The dHvA oscillations exhibit a forward-leaning sawtooth pattern, as illustrated by the dashed wave form. (c) Frequency spectrum of dHvA oscillations at different θ values. A major frequency of 140 T is observed at $\theta = 0^\circ$, which shifts to higher values at larger θ, as indicated by the dashed curve. The curves in (b) and (c) are offset, with (c) displayed on a logarithmic scale for clarity. (d) Color plot showing the angular dependence of Yb1. F_δ and F_ϕ nearly follow an $F_0/\cos\theta$ dependence, where F_0 is frequency at $\theta = 0^\circ$, as indicated by the dotted curves.

brilliant metallic luster and are easily exfoliated. We noted mild sensitivity of the samples to air and water. The detailed information about the sample synthesis and studies of the electrical and magnetic properties of $YbTi_3Bi_4$ have been reported in separate publications [39,42]. We used single crystals of this material from the same batch of the sample growth.

Torque measurements were performed using a miniature piezoresistive cantilever to observe dHvA oscillations. A selected single crystal of $YbTi_3Bi_4$ was attached to the cantilever arm using vacuum grease and then mounted on a rotating platform. The probe was slowly cooled to a base temperature of 0.5 K. Two resistive elements on the cantilever, along with two room-temperature resistors, formed a Wheatstone bridge that was balanced at the base temperature before sweeping the magnetic field. The sample was rotated *in situ* in applied fields at various tilt angles θ, where θ is the angle between the magnetic field and the c axis of the sample [inset in Fig. 2(a)]. Magnetic fields were swept at each fixed temperature at a rate of 1.5 T/min.

Electronic band and FS calculations were performed by using an open-source code Quantum Espresso (QE) [50], which is programed based on the density-function theory (DFT) formalism [51,52]. The unit-cell structure was relaxed without implementing constraints under vc-relax mode. To ensure the convergence of structural parameters and cell energies during structural optimization, the wave functions' kinetic energy and charge-density cutoffs were set to 70 and 750 Ry, respectively. The self-consistent iterative process was set to be 10^{-8} Ry to achieve the minimum total-energy difference convergence criteria.

III. RESULTS AND DISCUSSION

Figure 1(c) shows the torque τ for two $YbTi_3Bi_4$ single crystals (Yb1 and Yb2) with applied fields H up to 41.5 T at 0.5 K. The τ signal varies almost linearly with H and shows clear dHvA oscillations above 4 T. The dHvA oscillations are observed in both Yb1 and Yb2 samples. The oscillation signal is more pronounced in Yb1 than in Yb2 although both signals have the comparable frequency spectrum, as shown in the inset. It is important to note that the frequency spectra of Yb1 and Yb2 look similar, with both showing a major peak at $F_\delta = 142$ T. However, there are slight differences, especially in the frequencies near 700 T. This indicates that the Fermi levels of the two samples are slightly different. Therefore, we have presented detailed temperature- and angular-dependence data for Yb1 in the main text. To get frequency spectrum, we carried out background subtraction by fitting a smooth polynomial background and finally performed the fast Fourier transform (FFT). Figure 1(d) shows the frequency spectrum of Yb1 at different temperatures measured at $\theta = 28^\circ$. As shown in the graph, there is a dominant peak at $F_\delta = 142$ T, along with five other distinct peaks at 179 T, 535 T, 657 T, 810 T, and 969 T. Several smaller peaks, indicated by stars, are less pronounced and disappear quickly at temperatures above 2 K. Therefore, we have not taken them into consideration here. Furthermore, with careful analysis of the background subtraction, we resolved two high-frequency peaks near $F_\chi \sim 1900$ T and $F_\lambda \sim 5600$ T. We will discuss this in detail later. The amplitude of the dHvA oscillations decreases at higher temperatures and this behavior can be described by the Lifshitz-Kosevich (LK) theory [53]. The LK formula enables estimating the effective mass m^* of the charge carriers. According to this theory, the temperature dependence of dHvA oscillations is given by

$$\Delta\tau(T, H) \propto e^{-\lambda_D} \frac{\lambda(T/H)}{sinh[\lambda(T/H)]}, \quad (1)$$

with $\lambda_D(H) = \frac{2\pi^2 k_B}{\hbar e} m^* \frac{T_D}{H}$ and $\lambda(T/H) = \frac{2\pi^2 k_B}{\hbar e} m^* \frac{T}{H}$. Here, T_D, $\hbar$, and k_B represent the Dingle temperature, the reduced Plank's constant, and Boltzmann's constant, respectively. The first term is the Dingle factor, which describes the attenuation of the oscillations with decreasing field H. The second term explains the weakening of the oscillations at higher temperatures.

We have carried our LK analyses only for the major peak F_δ. Figure 1(e) shows the temperature dependence of the normalized FFT amplitudes of F_δ for Yb1 and Yb2 samples. The scattered data are experimental data while the solid curves are the best fits using the LK formula [Eq. (1)]. As seen in the figure, the LK theory fits temperature dependence of frequency data very well. From the best fitting, we have estimated $m^* = 0.135 m_o$ and $0.102 m_o$, where m_o is the free mass of electron, for Yb1 and Yb2, respectively. The m^* values for Yb1 and Yb2 are in good agreement with each other and are also comparable with the effective masses of other kagome compounds [30,38,54].

To determine other physical parameters of charge carriers, we have also conducted the Dingle temperature analyses for F_δ peak of both Yb1 and Yb2, as illustrated in the inset of Fig. 1(d). From the best fit curve, it is found that $T_D = (8.97 \pm 1.58)$ K and (11.93 ± 1.84) K, for Yb1 and Yb2, respectively. Using the value of T_D and m^*, we have estimated several parameters characterizing the Fermi pocket of F_δ. Taking Yb1 as an example, we used Onsager's relation [53], the frequency $f = \hbar/(2e)k_F^2$, and estimated the Fermi momentum corresponds to $k_F = 0.065 \text{Å}^{-1}$. Using the linear dispersion relation for the surface state $v_F = \hbar k_F / m^*$, we have estimated the Fermi velocity $v_F = 5.612 \times 10^5$ m s^{-1}. With the value of $T_D = 8.97$ K, the surface carrier life time $\tau = \hbar / 2\pi k_B T_D$ is estimated to be $\tau = 0.135 \times 10^{-12}$ s. Similarly, other physical parameters like the mean-free path $\ell_{2D} = v_F \tau$ and mobility $\mu = e\tau/m^*$ are estimated to be 7.57 nm and $0.176 m^2$ V^{-1} s^{-1}, respectively. The estimated FS parameters for both Yb1 and Yb2 are presented in Table I. As shown in the table, the parameters for Yb1 and Yb2 are in good agreement and comparable to those of other kagome and topological compounds [55–57].

According to Onsager's relation [53,58], the frequency of quantum oscillation is directly proportional to the cross section of the FS. Therefore, it is possible to map the FS by rotating the sample in the magnetic field. For this, we rotated the sample *in situ* magnetic field at different θ values. Angular dependence of torque data at selected θ values for Yb1 is shown in Fig. 2(a). While increasing angle, we can clearly see that the amplitude of oscillation changes. The oscillation is completely absent when the magnetic field is aligned along the *ab* plane, as shown in Figs. 2(a) and 2(b) ($\theta = 91^\circ$). The same feature is also observed in another sample, Yb1, as presented in Fig. S1 of the Supplemental Material (SM) [59]. The absence of dHvA oscillations at $\theta = 91^\circ$ strongly suggests the presence of a quasi-2D Fermi surface [60,61] in $YbTi_3Bi_4$.

It is noteworthy that dHvA oscillations [Fig. 2(b)] display a forward-leaning, sawtoothlike pattern at higher magnetic fields (above 20 T), with this feature becoming more pronounced at tilt angles (θ) greater than 28°, as indicated by the dashed line. A similar forward-leaning, sawtoothlike feature has also been observed in the Yb2 sample, as shown in Fig. S1(b) of SM [59]. This behavior is characteristic of ideal two-dimensional metals [62–64]. The forward-leaning sawtooth wave form arises from jumps in the chemical potential between discrete filled and empty Landau levels as the magnetic field is swept [63–65]. This sawtooth wave-form feature has recently been observed in torque measurements of underdoped cuprates [66] in pseudogap region, providing the evidence of a 2D Fermi pocket. Therefore, observation of such feature strongly suggests the presence of the 2D Fermi surface in $YbTi_3Bi_4$.

Figure 2(c) shows the frequency spectrum of $YbTi_3Bi_4$ at different θ values. As seen in the graph, the major frequency peak near 140 T at $\theta = 0^\circ$ gradually increases at higher angles, as indicated by the dashed curve. Due to the presence of multiple peaks in the frequency spectrum, we used a color plot to visualize the angle-dependent data [Fig. 2(d)]. The bright, intense color represents F_δ, which increases at higher angles. It appears that both F_δ and the frequency near $F_\phi = 620$ T exhibit an $F_0/\cos\theta$ dependence, where F_0 is the frequency value at $\theta = 0^\circ$, as indicated by the dotted curves. The dHvA oscillations observed in a second sample, Yb2, exhibit similar angular-dependence characteristics. A comprehensive analysis of the angular dependence for Yb2 is provided in Figures S1 and S2 of SM [59]. This $1/\cos\theta$ behavior strongly suggests the presence of cylindrical Fermi sheets in $YbTi_3Bi_4$.

To better understand the electronic properties of $YbTi_3Bi_4$ and explain experimental observation, we performed electronic band structure and FS calculations using *ab initio* DFT. Figure 3 displays the electronic band structure of $YbTi_3Bi_4$ along the high-symmetry direction shown in the inset. Our electronic bands look similar to previous reports [42,43,67] on LnTi$_3$Bi$_4$. The band structure reveals intriguing features, such as dispersionless flat bands at **A** and **X**, located around

TABLE I. Physical parameters of Yb1 and Yb2: the frequency (F), FS area (S_F), Fermi wave vector (k_F), effective mass (m^*), Fermi velocity (v_F), Dingle temperature T_D, quantum relaxation time (τ_s), mean-free path (ℓ_{2D}), and quantum mobility (μ), characterizing the dHvA oscillations of $YbTi_3Bi_4$.

Sample	F(T)	k_F(Å^{-1})	S_F(Å^{-2})	m^*/m_o	v_F(10^5 ms^{-1})	T_D(K)	τ_s(10^{-12} s)	ℓ_{2D} (nm)	μ(m^{2}V^{-1}s^{-1})
Yb1	142	0.065	1.354	0.135	5.612	8.97	0.135	7.57	0.176
Yb2	145	0.066	1.383	0.102	7.506	11.93	0.101	7.61	0.175

0.36 eV and 0.6 eV below the Fermi level, as highlighted by dashed arrows. Additionally, van Hove singularities (VHS) are present near **Y**, as indicated by arrows. Dirac-like crossings are observed near **A** and **X**, marked by dotted circles. Several bands cross the Fermi level, confirming the metallic nature of $YbTi_3Bi_4$.

There are five bands that cross the Fermi level and contribute to the FS. Figure 4 shows the band-resolved FS of $YbTi_3Bi_4$. The FS consists of five sheets originating from Bands 7, 8, 9, 10, and 11. The FSs of Bands 7, 8, and 9 are located at the corners of the Brillouin zone, while that of Band 10 is at the Γ point, and all of them appear cylindrical. Band 11 has two concavelike sheets facing upward and downward. These FS pockets resemble those in other V-based AV_3Sb_5 (A = Cs, K, Rb) and Ti-based $CsTi_3Bi_5$ Kagome systems [68,69]. The nearly two-dimensional nature of the FS indicates strong in-plane bonding and weak interlayer coupling in this material.

Figure 5(a) shows the Fermi surface of Band 7, Band 8, and Band 9 that are present at the Brillouin zone boundary. The presence of cylindrical FS sheets is consistent with the nearly $1/\cos\theta$ dependence of the frequency peaks in Fig. 2(d). We computed theoretical frequencies using the Onsager relationship [58]. We used the SKEAF code [70] to extract the theoretical frequencies from the FS cross-sectional area. Figures 5(b) and 5(c) present the frequencies derived from all FS sheets of $YbTi_3Bi_4$.

As shown in the graph, the FS of Band 7 contributes smaller frequencies of 150 T and 300 T compared to other bands; thus, it is plotted separately in Fig. 5(b). Additionally, the FS of Band 7 contributes the smallest frequency, approximately 170 T, which is also plotted separately in Fig. 5(b). As illustrated in Fig. 4, Band 10 exhibits a large cylindrical FS, resulting in a high frequency of 20 000 T. Similarly, the FSs of Bands 8 and 9 are cylindrical near the Brillouin zone boundary [Fig. 5(a)], contributing frequencies of approximately 2000 T and 5500 T, respectively, as shown in Fig. 5(c). The frequency associated with the FS of Band 11 is around 2000 T and decreases at higher θ values. Theoretical frequencies (except for Band 11) increase nearly parabolically with θ, consistent with expectations for cylindrical FSs.

For comparison with theoretical frequencies, we also included experimental frequencies derived from dHvA oscillations. In our dHvA data, we observed a major peak near $F_\delta \sim 130$ T. As shown in Fig. 5(b), F_δ and another peak near $F_\epsilon \sim 300$ T are consistent with the theoretical frequencies derived from the Fermi pocket of Band 7. Furthermore, F_δ and F_ϵ values extracted from Yb1 and Yb2 are comparable to the frequencies derived from Band 7, and they exhibit nearly the same angular dependence. To identify potential high-frequency signals in $YbTi_3Bi_4$, as predicted by theoretical calculations, we performed careful background subtraction and detected faint high-frequency signals near $F_\chi \sim 1900$ T and $F_\lambda \sim 5600$ T, as shown in Fig. S3 in SM [59]. These high frequencies were observed in both Yb1 and Yb2, confirming their intrinsic nature. As illustrated in Fig. 5(c), the values of F_χ and F_λ are comparable to the theoretical frequencies derived from Band 8 (or Band 11) and Band 9,

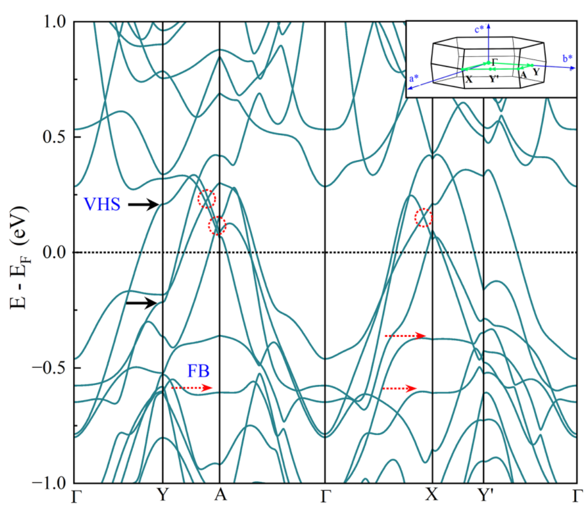

FIG. 3. Electronic band structure of $YbTi_3Bi_4$. The flat band, van-Hove singularity (VHS), and Dirac point near the Fermi level are denoted by the dashed-arrows, solid arrows, and dotted circles, respectively. Inset: Brillouin zone with high-symmetry k path.

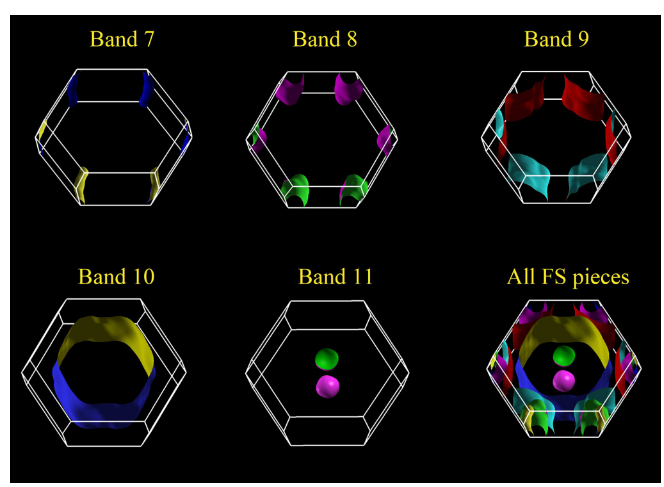

FIG. 4. Band-resolved Fermi surface (FS) pockets of $YbTi_3Bi_4$. There are five bands: Band 7, Band 8, Band 9, Band 10, and Band 11 contribute to the FS of $YbTi_3Bi_4$. The last graph is the combined FS contributions from all bands.

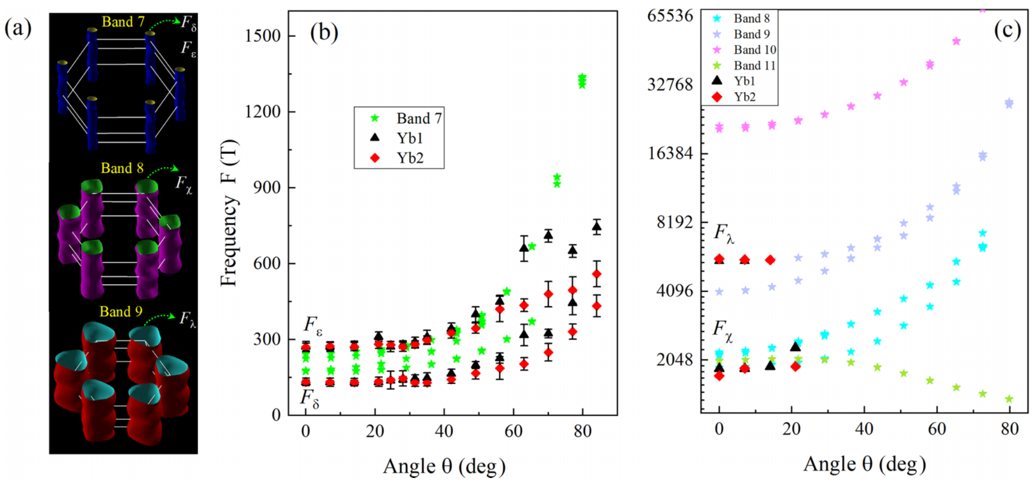

FIG. 5. (a) Fermi pockets for Bands 7, 8, and 9, showing their overall appearance. These pockets appear as deformed cylindrical shapes.(b) Comparison of experimental frequencies from dHvA oscillations with theoretical frequencies derived from the Fermi surface (FS) pocket of Band 7 for $YbTi_3Bi_4$. Solid circles and open triangles represent theoretical and experimental frequencies, respectively. (c) Frequencies calculated from the FS sheets of Bands 8, 9, 10, and 11 for $YbTi_3Bi_4$. The frequencies increase nearly parabolically, as expected for cylindrical FSs, except for Band 11, where the frequency decreases at higher angles. The *y* axis is presented on a logarithmic scale for better data visibility.

respectively. F_χ and F_λ are tiny signals and they are overshadowed by F_δ; therefore, we could not resolve them above $\theta = 21^\circ$. Increasing the magnetic field strength could improve the signal-to-noise ratio, potentially allowing for clearer resolution of these high-frequency peaks.

IV. SUMMARY

To summarize, we performed high-field torque magnetometry on the newly discovered Ti-based kagome material $YbTi_3Bi_4$. The torque signal exhibited well-defined de Haas–van Alphen (dHvA) oscillations, with a prominent peak F_δ around 140 T. By analyzing both angular and temperature-dependent dHvA oscillations, we extracted several key physical parameters that characterize the Fermi surface (FS) of F_δ. The observation of the characteristic forward-leaning sawtoothlike dHvA oscillations, combined with the $1/\cos\theta$ dependence of the dHvA signal, provides conclusive evidence for the presence of two-dimensional Fermi pockets in $YbTi_3Bi_4$.

In addition, we employed *ab initio* density-functional theory (DFT) calculations to explore the electronic band structure and FS of $YbTi_3Bi_4$. The electronic band structure revealed several intriguing features, including multiple Dirac points, van Hove singularities, and flat bands near the Fermi level. Five electronic bands intersect the Fermi level, contributing to a FS composed of quasi-2D cylindrical Fermi sheets. Theoretical frequencies derived from the Fermi surface of Band 7 are comparable to F_δ and exhibit a similar angular dependence. However, the frequencies derived from the Fermi surfaces of other bands are much higher, of the order of several kilo teslas. With the careful background subtraction in the dHvA oscillation, we could detect the additional frequency peaks near 1900 T and 5600 T, which are present in both measured samples Yb1 and Yb2, and are consistent with the theoretical frequencies derived from the Fermi pocket of 8 (or Band 11) and Band 9, respectively. These high-frequency peaks are very tiny and these signals quickly disappeared at higher tilt angles above 21°.

We noticed that F_δ splits at higher tilt angles (θ) above 60° [Fig. 2(c)] and this splitting is clearly visible in the color plot [Fig. 2(d)]. A similar splitting is also seen in another sample, Yb2, as shown in Fig. S2 SM [59]. This splitting is likely due to the contribution of different extremal orbits to the dHvA oscillations. In contrast to other kagome systems, such as AV_3Sb_5 and ATi_3Bi_5, the kagome lattice formed by Ti atoms in $YbTi_3Bi_4$ exhibits slight buckling. The Fermi pockets in this system also show a deformed, cylindrical-like shape with varying cross-sectional areas [see Fig. 4 and Fig. 5(a)]. As the tilt angle θ increases, the cyclotron orbit changes, leading to slightly different frequencies corresponding to the varying orientations of the Fermi surface.

Interestingly, our torque measurements reveal a forward-leaning triangular sawtoothlike wave-form pattern, strongly suggesting the presence of a quasi-2D Fermi surface. The angular dependence of F_δ follows a $1/\cos\theta$ dependence, which further supports the quasi-2D nature of the Fermi surface in $YbTi_3Bi_4$. These experimental findings are reinforced by the observation of cylindrical Fermi pockets and, importantly, the excellent agreement between the theoretical frequencies calculated from density-functional theory (DFT) and the experimental dHvA frequencies. The combined experimental and computational results for $YbTi_3Bi_4$ provide valuable insights into its electronic properties and will be crucial for understanding similar systems, including other members of the $LnTi_3Bi_4$ (Ln = Lanthanide) and other titanium- and vanadium-based kagome compounds.

ACKNOWLEDGMENTS

The work at the West Texas A&M University (WTAMU) is supported by the Welch Foundation (Grant No. AE-0025), and the National Science Foundation (Award ID 2336011). The computations were performed on the WTAMU HPC cluster, which was funded by the National Science Foundation (NSF CC* GROWTH 2018841). Work by B.R.O. is supported by the U.S. Department of Energy (DOE), Office of Science, Basic Energy Sciences (BES), Materials Sciences and Engineering Division. A portion of this work was performed at the National High Magnetic Field Laboratory, which is supported by National Science Foundation Cooperative Agreement No. DMR-2128556 and the State of Florida.

[1] L. Ye, M. Kang, J. Liu, F. von Cube, C. R. Wicker, T. Suzuki, C. Jozwiak, A. Bostwick, E. Rotenberg, D. C. Bell *et al.*, Massive Dirac fermions in a ferromagnetic kagome metal, Nature (London) **555**, 638 (2018).

[2] J.-X. Yin, W. Ma, T. A. Cochran, X. Xu, S. S. Zhang, H.-J. Tien, N. Shumiya, G. Cheng, K. Jiang, B. Lian *et al.*, Quantum-limit Chern topological magnetism in $TbMn_6Sn_6$, Nature (London) **583**, 533 (2020).

[3] K. Jiang, T. Wu, J.-X. Yin, Z. Wang, M. Z. Hasan, S. D. Wilson, X. Chen, and J. Hu, Kagome superconductors AV_3Sb_5 (A = K, Rb, Cs), Natl. Sci. Rev. **10**, nwac199 (2022).

[4] M. Mekata, Kagome: The story of the basketweave lattice, Phys. Today **56**, 12 (2003).

[5] B. R. Ortiz, L. C. Gomes, J. R. Morey, M. Winiarski, M. Bordelon, J. S. Mangum, I. W. H. Oswald, J. A. Rodriguez-Rivera, J. R. Neilson, S. D. Wilson *et al.*, New kagome prototype materials: Discovery of KV_3Sb_5, RbV_3Sb_5, and CsV_3Sb_5, Phys. Rev. Mater. **3**, 094407 (2019).

[6] B. R. Ortiz, P. M. Sarte, E. M. Kenney, M. J. Graf, S. M. L. Teicher, R. Seshadri, and S. D. Wilson, Superconductivity in the $\mathbb{Z}_2$ kagome metal KV_3Sb_5, Phys. Rev. Mater. **5**, 034801 (2021).

[7] B. R. Ortiz, S. M. Teicher, Y. Hu, J. L. Zuo, P. M. Sarte, E. C. Schueller, A. M. Abeykoon, M. J. Krogstad, S. Rosenkranz, R. Osborn *et al.*, CsV_3Sb_5: A $\mathbb{Z}_2$ topological kagome metal with a superconducting ground state, Phys. Rev. Lett. **125**, 247002 (2020).

[8] F. H. Yu, D. H. Ma, W. Z. Zhuo, S. Q. Liu, X. K. Wen, B. Lei, J. J. Ying, and X. H. Chen, Unusual competition of superconductivity and charge-density-wave state in a compressed topological kagome metal, Nat. Commun. **12**, 3645 (2021).

[9] K. Y. Chen, N. N. Wang, Q. W. Yin, Y. H. Gu, K. Jiang, Z. J. Tu, C. S. Gong, Y. Uwatoko, J. P. Sun, H. C. Lei *et al.*, Double superconducting dome and triple enhancement of T_c in the kagome superconductor CsV_3Sb_5 under high pressure, Phys. Rev. Lett. **126**, 247001 (2021).

[10] N. N. Wang, K. Y. Chen, Q. W. Yin, Y. N. N. Ma, B. Y. Pan, X. Yang, X. Y. Ji, S. L. Wu, P. F. Shan, S. X. Xu *et al.*, Competition between charge-density-wave and superconductivity in the kagome metal RbV_3Sb_5, Phys. Rev. Res. **3**, 043018 (2021).

[11] M. Kang, S. Fang, J.-K. Kim, B. R. Ortiz, S. H. Ryu, J. Kim, J. Yoo, G. Sangiovanni, D. D. Sante, B.-G. Park *et al.*, Twofold van Hove singularity and origin of charge order in topological kagome superconductor CsV_3Sb_5, Nat. Phys. **18**, 301 (2022).

[12] S. D. Wilson and B. R. Ortiz, Av_3Sb_5 kagome superconductors, Nat. Rev. Mater. **9**, 420 (2024).

[13] F. H. Yu, T. Wu, Z. Y. Wang, B. Lei, W. Z. Zhuo, J. J. Ying, and X. H. Chen, Concurrence of anomalous Hall effect and charge density wave in a superconducting topological kagome metal, Phys. Rev. B **104**, L041103 (2021).

[14] Q. Yin, Z. Tu, C. Gong, Y. Fu, S. Yan, and H. Lei, Superconductivity and normal-state properties of kagome metal RbV_3Sb_5 single crystals, Chin. Phys. Lett. **38**, 037403 (2021).

[15] S.-Y. Yang, Y. Wang, B. R. Ortiz, D. Liu, J. Gayles, E. Derunova, R. Gonzalez-Hernandez, L. Šmejkal, Y. Chen, S. S. P. Parkin, S. D. Wilson, E. S. Toberer, and T. M. M. N. Ali, Giant, unconventional anomalous Hall effect in the metallic frustrated magnet candidate, KV_3Sb_5, Sci. Adv. **6**, eabb6003 (2020).

[16] K. Nakayama, Y. Li, T. Kato, M. Liu, Z. Wang, T. Takahashi, Y. Yao, and T. Sato, Carrier injection and manipulation of charge-density wave in kagome superconductor CsV_3Sb_5, Phys. Rev. X **12**, 011001 (2022).

[17] B. R. Ortiz, S. M. L. Teicher, L. Kautzsch, P. M. Sarte, N. Ratcliff, J. Harter, J. P. C. Ruff, R. Seshadri, and S. D. Wilson, Fermi surface mapping and the nature of charge-density-wave order in the kagome superconductor CsV_3Sb_5, Phys. Rev. X **11**, 041030 (2021).

[18] H. Luo, Q. Gao, H. Liu, Y. Gu, D. Wu, C. Yi, J. Jia, S. Wu, X. Luo, Y. Xu *et al.*, Electronic nature of charge density wave and electron-phonon coupling in kagome superconductor KV_3Sb_5, Nat. Commun. **13**, 273 (2022).

[19] Y. Fu, N. Zhao, Z. Chen, Q. Yin, Z. Tu, C. Gong, C. Xi, X. Zhu, Y. Sun, K. Liu *et al.*, Quantum transport evidence of topological band structures of kagome superconductor CsV_3Sb_5, Phys. Rev. Lett. **127**, 207002 (2021).

[20] W. Zhang, L. Wang, C. W. Tsang, X. Liu, J. Xie, W. C. Yu, K. T. Lai, and S. K. Goh, Emergence of large quantum oscillation frequencies in thin flakes of the kagome superconductor CsV_3Sb_5, Phys. Rev. B **106**, 195103 (2022).

[21] C. Broyles, D. Graf, H. Yang, X. Dong, H. Gao, and S. Ran, Effect of the interlayer ordering on the Fermi surface of kagome superconductor CsV_3Sb_5 revealed by quantum oscillations, Phys. Rev. Lett. **129**, 157001 (2022).

[22] K. Shrestha, M. Shi, T. Nguyen, D. Miertschin, K. Fan, L. Deng, D. E. Graf, X. Chen, and C.-W. Chu, Fermi surface mapping of the kagome superconductor RbV_3Sb_5 using de Haas-van Alphen oscillations, Phys. Rev. B **107**, 075120 (2023).

[23] K. Shrestha, R. Chapai, B. K. Pokharel, D. Miertschin, T. Nguyen, X. Zhou, D. Y. Chung, M. G. Kanatzidis, J. F. Mitchell, U. Welp *et al.*, Nontrivial Fermi surface topology of the kagome superconductor CsV_3Sb_5 probed by de Haas–van Alphen oscillations, Phys. Rev. B **105**, 024508 (2022).

[24] G. Pokharel, S. M. L. Teicher, B. R. Ortiz, P. M. Sarte, G. Wu, S. Peng, J. He, R. Seshadri, and S. D. Wilson, Electronic properties of the topological kagome metals YV_6Sn_6 and GdV_6Sn_6, Phys. Rev. B **104**, 235139 (2021).

[25] J. Lee and E. Mun, Anisotropic magnetic property of single crystals RV_6Sn_6(R = Y, Gd−Tm, Lu), Phys. Rev. Mater. **6**, 083401 (2022).

[26] S. Peng, Y. Han, G. Pokharel, J. Shen, Z. Li, M. Hashimoto, D. Lu, B. R. Ortiz, Y. Luo, H. Li *et al.*, Realizing kagome band structure in two-dimensional kagome surface states of RV_6Sn_6 (R = Gd, Ho), Phys. Rev. Lett. **127**, 266401 (2021).

[27] E. Rosenberg, J. M. DeStefano, Y. Guo, J. S. Oh, M. Hashimoto, D. Lu, R. J. Birgeneau, Y. Lee, L. Ke, M. Yi *et al.*, Uniaxial

ferromagnetism in the kagome metal TbV_6Sn_6, Phys. Rev. B **106**, 115139 (2022).

[28] X. Zhang, Z. Liu, Q. Cui, Q. Guo, N. Wang, L. Shi, H. Zhang, W. Wang, X. Dong, J. Sun *et al.*, Electronic and magnetic properties of intermetallic kagome magnets $RV_6Sn_6(R = \mathrm{Tb}-\mathrm{Tm})$, Phys. Rev. Mater. **6**, 105001 (2022).

[29] G. Pokharel, B. Ortiz, J. Chamorro, P. Sarte, L. Kautzsch, G. Wu, J. Ruff, and S. D. Wilson, Highly anisotropic magnetism in the vanadium-based kagome metal TbV_6Sn_6, Phys. Rev. Mater. **6**, 104202 (2022).

[30] K. Shrestha, B. Regmi, G. Pokharel, S.-G. Kim, S. D. Wilson, D. E. Graf, B. A. Magar, C. Phillips, and T. Nguyen, Electronic properties of kagome metal ScV_6Sn_6 using high-field torque magnetometry, Phys. Rev. B **108**, 245119 (2023).

[31] H. W. S. Arachchige, W. R. Meier, M. Marshall, T. Matsuoka, R. Xue, M. A. McGuire, R. P. Hermann, H. Cao, and D. Mandrus, Charge density wave in kagome lattice intermetallic ScV_6Sn_6, Phys. Rev. Lett. **129**, 216402 (2022).

[32] Y. Hu, X. Wu, Y. Yang, S. Gao, N. C. Plumb, A. P. Schnyder, W. Xie, J. Ma, and M. Shi, Tunable topological Dirac surface states and van Hove singularities in kagome metal GdV_6Sn_6, Sci. Adv. **8**, eadd2024 (2022).

[33] T. Hu, H. Pi, S. Xu, L. Yue, Q. Wu, Q. Liu, S. Zhang, R. Li, X. Zhou, J. Yuan *et al.*, Optical spectroscopy and band structure calculations of the structural phase transition in the vanadium-based kagome metal ScV_6Sn_6, Phys. Rev. B **107**, 165119 (2023).

[34] X. Zhang, J. Hou, W. Xia, Z. Xu, P. Yang, A. Wang, Z. Liu, J. Shen, H. Zhang, X. Dong *et al.*, Destabilization of the charge density wave and the absence of superconductivity in ScV_6Sn_6 under high pressures up to 11 gpa, Materials **15**, 7372 (2022).

[35] B. R. Ortiz, W. R. Meier, G. Pokharel, J. Chamorro, F. Yang, S. Mozaffari, A. Thaler, S. J. G. Alvarado, H. Zhang, D. S. Parker *et al.*, Stability frontiers in the AM_6X_6 kagome metals; The $LnNb_6Sn_6$(Ln: Ce-Lu, Y) family and density-wave transition in $LuNb_6Sn_6$, arXiv:2411.10635.

[36] D. Werhahn, B. R. Ortiz, A. K. Hay, S. D. Wilson, R. Seshadri, and D. Johrendt, The kagomé metals $RbTi_3Bi_5$ and $CsTi_3Bi_5$, Z. Naturforsch. B **77**, 757 (2022).

[37] X.-W. Yi, X.-Y. Ma, Z. Zhang, Z.-W. Liao, J.-Y. You, and G. Su, Large kagome family candidates with topological superconductivity and charge density waves, Phys. Rev. B **106**, L220505 (2022).

[38] Z. Rehfuss, C. Broyles, D. Graf, Y. Li, H. Tan, Z. Zhao, J. Liu, Y. Zhang, X. Dong, H. Yang *et al.*, Quantum oscillations in kagome metals $CsTi_3Bi_5$ and $RbTi_3Bi_5$, Phys. Rev. Mater. **8**, 024003 (2024).

[39] B. R. Ortiz, H. Miao, D. S. Parker, F. Yang, G. D. Samolyuk, E. M. Clements, A. Rajapitamahuni, T. Yilmaz, E. Vescovo, J. Yan *et al.*, Evolution of highly anisotropic magnetism in the titanium-based kagome metals $LnTi_3Bi_4$ (Ln: La Gd^{3+}, Eu^{2+}, Yb^{2+}), Chem. Mater. **35**, 9756 (2023).

[40] B. R. Ortiz, H. Zhang, K. Górnicka, D. S. Parker, G. D. Samolyuk, F. Yang, H. Miao, Q. Lu, R. G. Moore, A. F. May *et al.*, Intricate magnetic landscape in antiferromagnetic kagome metal $TbTi_3Bi_4$ and interplay with $Ln_{2-x}Ti_6 + xBi_9$ (Ln: Tb Lu) shurikagome metals, Chem. Mater. **36**, 8002 (2024).

[41] M. I. Mondal, A. P. Sakhya, M. Sprague, B. R. Ortiz, M. Matzelle, B. Ghosh, N. Valadez, I. B. Elius, A. Bansil, and M. Neupane, Observation of multiple van Hove singularities and correlated electronic states in a new topological ferromagnetic kagome metal $NdTi_3Bi_4$, arXiv:2311.11488.

[42] A. P. Sakhya, B. R. Ortiz, B. Ghosh, M. Sprague, M. I. Mondal, M. Matzelle, I. Bin Elius, N. Valadez, D. G. Mandrus, A. Bansil *et al.*, Diverse electronic landscape of the kagome metal $YbTi_3Bi_4$, Commun. Mater. **5**, 241 (2024).

[43] Y. Hu, C. Le, L. Chen, H. Deng, Y. Zhou, N. C. Plumb, M. Radovic, R. Thomale, A. P. Schnyder, J.-X. Yin *et al.*, Magnetic coupled electronic landscape in bilayer-distorted titanium-based kagome metals, Phys. Rev. B **110**, L121114 (2024).

[44] Z. Jiang, T. Li, J. Yuan, Z. Liu, Z. Cao, S. Cho, M. Shu, Y. Yang, J. Ding, Z. Li *et al.*, Direct observation of topological surface states in the layered kagome lattice with broken time-reversal symmetry, arXiv:2309.01579.

[45] E. Cheng, K. Wang, S. Nie, T. Ying, Z. Li, Y. Li, Y. Xu, H. Chen, R. Koban, H. Borrmann *et al.*, Spectroscopic origin of giant anomalous Hall effect in an interwoven magnetic kagome metal, arXiv:2405.16831.

[46] Z. Zheng, L. Chen, X. Ji, Y. Zhou, G. Qu, M. Hu, Y. Huang, H. Weng, T. Qian, and G. Wang, Anisotropic magnetism and band evolution induced by ferromagnetic phase transition in titanium-based kagome ferromagnet $SmTi_3Bi_4$, Sci. China: Phys. Mech. Astron. **67**, 267411 (2024).

[47] L. Chen, Y. Zhou, H. Zhang, X. Ji, K. Liao, Y. Ji, Y. Li, Z. Guo, X. Shen, R. Yu *et al.*, Tunable magnetism in titanium-based kagome metals by rare-earth engineering and high pressure, Commun. Materials **5**, 73 (2024).

[48] J. Guo, L. Zhou, J. Ding, G. Qu, Z. Liu, Y. Du, H. Zhang, J. Li, Y. Zhang, F. Zhou *et al.*, Tunable magnetism and band structure in kagome materials $ReTi_3Bi_4$ family with weak interlayer interactions, Sci. Bull. **69**, 2660 (2024).

[49] P. C. Canfield, T. Kong, U. S. Kaluarachchi, and N. H. Jo, Use of frit-disc crucibles for routine and exploratory solution growth of single crystalline samples, Philos. Mag. **96**, 84 (2016).

[50] P. Giannozzi, S. Baroni, N. Bonini, M. Calandra, R. Car, C. Cavazzoni, D. Ceresoli, G. L. Chiarotti, M. Cococcioni, I. Dabo *et al.*, QUANTUM ESPRESSO: A modular and open-source software project for quantum simulations of materials, J. Phys.: Condens. Matter **21**, 395502 (2009).

[51] W. Kohn and L. J. Sham, Self-consistent equations including exchange and correlation effects, Phys. Rev. **140**, A1133 (1965).

[52] P. Hohenberg and W. Kohn, Inhomogeneous electron gas, Phys. Rev. **136**, B864 (1964).

[53] D. Shoenberg, *Magnetic Oscillations in Metals* (Cambridge University Press, Cambridge, UK, 1984).

[54] G. Zheng, Y. Zhu, S. Mozaffari, N. Mao, K.-W. Chen, K. Jenkins, D. Zhang, A. Chan, H. W. S. Arachchige, R. P. Madhogaria *et al.*, Quantum oscillations evidence for topological bands in kagome metal ScV_6Sn_6, J. Phys.: Condens. Matter **36**, 215501 (2024).

[55] M. He, X. Xu, D. Li, Q. Zeng, Y. Liu, H. Zhao, S. Zhou, J. Zhou, and Z. Qu, Quantum oscillations in the kagome metals (Ti,Zr,Hf)V_6Sn_6 at van Hove filling, Phys. Rev. B **109**, 155117 (2024).

[56] K. Shrestha, V. Marinova, D. Graf, B. Lorenz, and C. W. Chu, Quantum oscillations in metallic Sb_2Te_2Se topological insulator, Phys. Rev. B **95**, 075102 (2017).

[57] D. Miertschin, T. Nguyen, S. R. Bhandari, K. Shtefiienko, C. Phillips, B. A. Magar, R. Sankar, D. E. Graf, and K. Shrestha, Anisotropic quantum transport in ZrSiS probed by high-field torque magnetometry, Phys. Rev. B **110**, 085140 (2024).

[58] According to the Onsager's relation, the quantum oscillation measured frequency of an electron orbit (F) which is perpendicular to the applied magnetic field is related to the area of the Fermi surface (A) by $F = \frac{\phi_0}{2\pi^2}A$ where $\phi_0 = 2.07 \times 10^{-15}$ T.m^2 is the quantum of flux.

[59] See Supplemental Material at http://link.aps.org/supplemental/10.1103/PhysRevB.111.035145 for the angle dependent de Haas-van Alphen (dHvA) oscillations data and their frequency analyes of $YbTi_3Bi_4$.

[60] Y. Ando, Topological insulator materials, J. Phys. Soc. Jpn. **82**, 102001 (2013).

[61] A. A. Taskin and Y. Ando, Berry phase of nonideal Dirac fermions in topological insulators, Phys. Rev. B **84**, 035301 (2011).

[62] J. Eisenstein, H. Stormer, V. Narayanamurti, A. Cho, A. Gossard, and C. Tu, Density of states and de Haas—van Alphen effect in two-dimensional electron systems, Phys. Rev. Lett. **55**, 875 (1985).

[63] N. Harrison, R. Bogaerts, P. Reinders, J. Singleton, S. Blundell, and F. Herlach, Numerical model of quantum oscillations in quasi-two-dimensional organic metals in high magnetic fields, Phys. Rev. B **54**, 9977 (1996).

[64] D. Shoenberg, Magnetization of a two-dimensional electron gas, J. Low Temp. Phys. **56**, 417 (1984).

[65] K. Jauregui, V. Marchenko, and I. Vagner, Magnetization of a two-dimensional electron gas, Phys. Rev. B **41**, 12922 (1990).

[66] M. Hartstein, Y.-T. Hsu, K. A. Modic, J. Porras, T. Loew, M. L. Tacon, H. Zuo, J. Wang, Z. Zhu, M. K. Chan *et al.*, Hard antinodal gap revealed by quantum oscillations in the pseudogap regime of underdoped high-T_c superconductors, Nat. Phys. **16**, 841 (2020).

[67] M. I. Mondal, A. P. Sakhya, M. Sprague, B. R. Ortiz, M. Matzelle, B. Ghosh, N. Valadez, I. B. Elius, A. Bansil, and M. Neupane, Observation of multiple van Hove singularities and correlated electronic states in a new topological ferromagnetic kagome metal $NdTi_3Bi_4$, arXiv:2311.11488.

[68] K. Shrestha, M. Shi, B. Regmi, T. Nguyen, D. Miertschin, K. Fan, L. Z. Deng, N. Aryal, S.-G. Kim, D. E. Graf, X. Chen, and C. W. Chu, High quantum oscillation frequencies and nontrivial topology in kagome superconductor KV_3Sb_5 probed by torque magnetometry up to 45 T, Phys. Rev. B **107**, 155128 (2023).

[69] J. Yang, X. Yi, Z. Zhao, Y. Xie, T. Miao, H. Luo, H. Chen, B. Liang, W. Zhu, Y. Ye *et al.*, Observation of flat band, Dirac nodal lines and topological surface states in kagome superconductor $CsTi_3Bi_5$, Nat. Commun. **14**, 4089 (2023).

[70] P. M. C. Rourke, Numerical extraction of de Haas–van Alphen frequencies from calculated band energies, Comput. Phys. Commun. **183**, 324 (2012).